Dyes and Pigments 131 (2016) 160–167

Contents lists available at ScienceDirect

Dyes and Pigments

journal homepage: www.elsevier.com/locate/dyepig

Synthesis and properties of a novel narrow band gap oligomeric diketopyrrolopyrrole-based organic semiconductor

Mylène Le Borgne [a, b, c, d], Jesse Quinn [d], Jaime Martín [e], Natalie Stingelin [e], Guillaume Wantz [a, b, c, **], Yuning Li [d, *]

[a] University of Bordeaux, IMS, UMR 5218, F-33400, Talence, France
[b] CNRS, IMS, UMR 5218, F-33400, Talence, France
[c] Bordeaux INP, IMS, UMR 5218, F-33400, Talence, France
[d] Dept of Chemical Engineering, University of Waterloo, 200 University Ave West, Waterloo, ON, N2L 3G1, Canada
[e] Dept of Materials and Centre for Plastic Electronics, Imperial College London, London, UK

ARTICLE INFO

Article history:
Received 9 January 2016
Received in revised form
16 March 2016
Accepted 1 April 2016
Available online 2 April 2016

Keywords:
Organic solar cells
Organic semiconductors
Oligomers
Organic thin film transistors
Nanophase separation
Morphology

ABSTRACT

A trimer of diketopyrrolopyrole (DPP), Tri-BTDPP, was synthesized and characterized. Tri-BTDPP has a HOMO level of −5.34 eV, a low band gap of 1.33 eV, and a hole mobility of ~10^{-3} cm^2 V^{-1} s^{-1} in organic field effect transistors (OFETs). Organic photovoltaic (OPV) devices using the donor/acceptor blends of Tri-BTDPP and $PC_{71}BM$ exhibited low power conversion efficiencies (PCE) of up to 0.72%, even though the desirable optical and electronic characteristics of this compound as a donor semiconductor for achieving high performance for OPV. Through an intensive study of the active layer using AFM, XRD, and DSC, it was found that Tri-BTDPP and $PC_{71}BM$ were unable to intermix and formed oversized Tri-BTDPP phases, resulting in poor charge separation. Some guidance on how to improve the OPV performance of Tri-DPP compounds is provided.

1. Introduction

Organic photovoltaics (OPVs) or organic solar cells represent a promising technology to provide sustainable and cost-effective energy because OPVs can be manufactured at high throughputs using printing technologies. They have attracted enormous attention from the scientific community and industry for the last decade [1–9]. Depending on the molecular weight, the organic semiconductors used in OPVs can be either polymers or small molecules, both of which have achieved high power conversion efficiencies (PCE) of about 10% in single-junction devices [10–13]. Small molecule organic semiconductors have well-defined structures and much higher purity than their polymer counterparts. Their syntheses do not suffer from large batch-to-batch variations as those of polymers. However, solution-processed small molecules often show poor film formation capability compared to polymers. Consequently, OPVs based on solution-processed small molecules often have low fill factors (FFs). To improve the solution processability while maintaining other merits of small molecules, oligomeric organic semiconductors with molecular weights between those of polymers and small molecules are being studied recently. Power conversion efficiencies (PCE) of 6–9% have been achieved with oligomer semiconductors [14–16], which are comparable to those of small molecule [1–4] and polymer solar cells [17–19].

Diketopyrrolopyrrole (DPP) derivatives such as Pigment Red 254 (C.I.56110) are well known dyes and pigments [20]. DPP is currently one of the most widely studied electron-accepting building blocks for constructing low band gap semiconductors including small molecules, oligomers, and polymers for OPVs [21–30]. A series of oligomers consisting of two DPP terminal units and different cores such as naphtodithiophene and benzodithiophene (DPP-Core-DPP) were reported to achieve a PCE of 4–5% [25,26]. In 2013, Nguyen's group reported Tri-DPP (DPP-DPP-DPP) having one bisphenyl DPP unit flanked by two bisthiophene DPP units [22,31], which showed improved charge transport, quality of the film, FF and PCE (5.5%) of

* Corresponding author.
** Corresponding author. University of Bordeaux, IMS, UMR 5218, F-33400, Talence, France.
E-mail addresses: guillaume.wantz@ims-bordeaux.fr (G. Wantz), yuning.li@uwaterloo.ca (Y. Li).

http://dx.doi.org/10.1016/j.dyepig.2016.04.002
0143-7208/

the OPV devices. It is known that bisphenyl DPP unit is non-coplanar with a large dihedral angle of ~20–40° due to the steric repulsion between the phenyl ring and the DPP core [30]. Here, we report a new DPP oligomer consisting of three bisthiophene DPP units in order to achieve a coplanar structure. A coplanar molecular geometry is expected to contribute to greater crystallinity, improved charge transport, and a lower band gap of the semiconductor. We used this new DPP compound as an electron donor (combined with [6,6]-phenyl-C_{71}-butyric acid methyl ester ($PC_{71}BM$) as electron acceptor) in OPV devices.

2. Experimental section

2.1. Materials and measurements

All reagents and chemicals were purchased from commercial sources and used without further purification. 3-(5-Bromothiophen-2-yl)-2,5-bis(2-ethylhexyl)-6-(thiophen-2-yl)-2,5-dihydropyrrolo [3,4-*c*]pyrrole-1,4-dione (**1**) and 2,5-bis(2-octyldodecyl)-3,6-bis(5-(trimethylstannyl)thiophen-2-yl)-2,5-dihydropyrrolo [3,4-*c*]pyrrole-1,4-dione (**2**) were prepared as described in the literature [32,33].

^{1}H NMR and ^{13}C NMR spectra were recorded on 400 MHz and 300 MHz Bruker NMR using $CDCl_3$ as solvent and tetramethylsilane (TMS, 0 ppm) as a reference. High resolution electrospray technique mass spectrometry was used for Tri-BTDPP and MALDI-TOF for the by-product. Cyclic voltammetry (CV) measurements were conducted using a DY2000EN electrochemical workstation in a 0.1 M tetrabutylammonium hexafluorophosphate electrolyte solution in acetonitrile at room temperature at a scan rate of 50 mV s^{-1}. The working electrode and counter electrode were platinum electrodes and the reference electrode was Ag/AgCl (0.1 M) electrode. The reference electrode was calibrated against the redox potential of ferrocene/ferrocenium (Fc/Fc^+). A Pt disk with a semiconductor thin film formed by drop-casting a chloroform solution was used as the working electrode. AFM imaging was carried out at room temperature using an AFM Nanoman from Bruker Instrument with Nanoscope 5 controller. Images were obtained in tapping mode using silicon tips (PointProbe® Plus AFM-probe, Nanosensors, Switzerland). Differential scanning calorimetry (DSC) was performed on a Mettler–Toledo DSC 1 Stare system at a heating/cooling rate of 10 °C min^{-1}. The molecular packing was characterized by wide-angle X-ray diffraction (XRD, PANalytical X'Pert Pro MPD) using the Cu Kα radiation. θ/2θ scans were performed to the drop cast films at room temperature.

2.2. Device and characterization

The photovoltaic properties were tested in both conventional solar cells and inverted solar cells adopting respectively the structures of ITO/PEDOT:PSS/Tri:BTDPP:$PC_{71}BM$/(Ca)/Al and ITO/ZnOx/TriBTDPP:$PC_{71}BM$/MoO_3/Ag. For conventional solar cells fabrication, ITO–coated glass substrates were successively cleaned in ultrasonic baths of acetone/ethanol/isopropanol for 10 min, followed by oxygen plasma treatment for 15 min. An aqueous solution of PEDOT:PSS, previously filtrated with a 0.2 μm filter, was deposited by spin-coating at 4000 rpm for 60 s. The layer was dried in an oven at 100 °C under vacuum for 30 min. Then, a solution of Tri-BTDPP:$PC_{71}BM$ (1:1, 15 mg mL^{-1}) in chloroform containing optional 1 vol.% DIO were spin-coated on top of PEDOT:PSS under nitrogen atmosphere. The thickness of the active layer was ~90 nm. The solvents were removed by annealing the active layer at 80 °C for 10 min. Calcium (10 nm) and then aluminum (80 nm) were thermally evaporated onto the active layer through shadow masks under 2–4 × 10^{-6} mbar. The effective area was 10 mm^2.

For inverted solar cell, after similarly pre-cleaning the ITO-coated substrates, a solution of ZnO_x prepared with 0.15 M of zinc acetate and 0.15 M of ethanol amine in ethanol was spin-coated at 2000 rpm for 60 s. The layer was annealed at 180 °C for 1 h. The active layer was prepared and deposited as for the conventional solar cells. To complete the device, molybdenum (IV) oxide (10 nm) and silver (80 nm) were thermally evaporated onto the active layer through shadow masks under 2–4 × 10^{-6} mbar. The effective area was 10 mm^2.

The devices were characterized using a K.H.S SolarCelltest-575 solar simulator with AM 1.5G filters set at 100 mW cm^{-2} with a calibrated radiometer (IL 1400BL). The current density-voltage (J-V) curves were measured with Labview controlled Keithley 2400 SMU. Devices were characterized under nitrogen in a set of glove boxes (O_2 and H_2O < 0.1 ppm).

Bottom-gate, bottom-contact field effect transistors (OFETs) were fabricated using Fraunhofer IPMS templates of heavily n-doped Si with 200 nm-thick silicon oxide and gold electrodes. Substrates were cleaned with successive acetone and IPA baths followed by 15 min of UV-ozone treatment. A solution of 5 mg mL^{-1} of Tri-BTDPP in chloroform was spin-coated at 2500 rpm for 40 s on top of transistor substrates in the nitrogen-filled glovebox to form a 40 nm-thick layer. The dimensions of the channel were L = 5 μm and W = 1 cm. Transistors were measured using a semiconductor analyzer (Keithley 4200) coupled with a probe station.

2.3. Synthesis

2.3.1. 6,6′-((2,5-Bis(2-octyldodecyl)-3,6-dioxo-2,3,5,6-tetrahydropyrrolo[3,4-c]pyrrole-1,4-diyl)bis([2,2′-bisthiophene]-5′,5-diyl))bis(2,5-bis(2-ethylhexyl)-3-(thiophen-2-yl)-2,5-dihydropyrrolo[3,4-c]pyrrole-1,4-dione) (Tri-BTDPP)

A 100 mL dry three-necked round bottom flask was charged with compound **1** (1.5 g, 0.0025 mol, 2.1 eq), compound **2** (1.40 g, 0.0012 mol, 1 eq), P(*o*-tolyl)$_3$ (28.7 mg, 0.09 mmol, 0.08 eq) and anhydrous toluene (49 mL) under argon. Then, $Pd_2(dba)_3$ (21.9 mg, 0.024 mmol, 0.02 eq) dissolved in anhydrous toluene (1 mL) was added into the flask through a syringe. The mixture was heated to reflux and the color of the solution turned from purple to blue gradually. The reaction was monitored by the thin layer chromatography (TLC) analysis of the reaction mixture. After 60 h, no appreciable starting materials were detected and the reaction was terminated by cooling the reaction mixture to room temperature. The solution was poured into methanol (600 mL) and stirred for 30 min. The resulting precipitate was filtered and purified using column chromatography on silica gel with a mixture of dichloromethane (DCM) and hexane (with a volume ratio of 6:4) and then pure chloroform as eluent to afford 1.65 g (72%) of the crude product and 0.60 g (26%) of 6,6′-([2,2′-bithiophene]-5,5′-diyl) bis(2,5-bis(2-ethylhexyl)-3-(thiophen-2-yl)-2,5-dihydropyrrolo [3,4-*c*]pyrrole-1,4-dione) (**3**), a by-product formed by the mono-coupling of compound **1** and **2**. The crude product obtained by the first column separation contains the target Tri-BTDPP and the by-product 3-(5′-(2,5-bis(2-ethylhexyl)-3,6-dioxo-4-(thiophen-2-yl)-2,3,5,6-tetrahydropyrrolo[3,4-c]pyrrol-1-yl)-[2,2′-bithiophen]-5-yl)-2,5-bis(2-octyldodecyl)-6-(thiophen-2-yl)-2,5-dihydropyrrolo[3,4-*c*]pyrrole-1,4-dione (**4**), formed by the homo-coupling of **1**. 0.50 g of this crude product was further purified on silica gel column chromatography at 50 °C using a mixture of chloroform/toluene (volume ratio: 1/1) as eluent to afford 0.39 g pure Tri-BTDPP as a dark blue solid and 0.11 g of the by-product **4**. The total amounts of Tri-BTDPP and **4** in 1.65 g of the crude product are estimated to be 1.29 g (56%) and 0.36 g (16%), respectively. Data for Tri-BTDPP: ^{1}δH NMR ($CDCl_3$, 400 MHz) 8.93 (2H, d, J = 4.2 Hz), 8.91 (2H, d, J = 4.2 Hz), 8.85 (2H, dd, J = 3.9, 1.1 Hz), 7.49 (2H, dd,

J = 5.0, 1.0 Hz), 7.25 (4H, dd, J = 3.9, 3.5 Hz), 7.14 (2H, dd, J = 4.9, 4.0 Hz), 3.96 (12H, d, J = 5.2 Hz), 2.00–1.71 (6H, m), 1.39–1.23 (35H, m), 1.22–1.05 (70H, m), 0.92–0.72 (41H, m). ^{13}δC NMR ($CDCl_3$,400 MHz) 161.81, 161.69, 141.49, 141.19, 140.67, 139.33, 139.28, 137.43, 137.15, 135.95, 131.03, 130.14, 130.02, 129.95, 128.77, 126.12, 109.37, 109.08, 108.44, 77.56, 46.76, 46.30, 39.73, 39.46, 38.41, 32.26, 32.24, 31.60, 30.68, 30.56, 30.51, 30.45, 30.05, 29.99, 29.97, 29.92, 29.72, 29.70, 28.84, 28.69, 26.65, 24.02, 23.87, 23.47, 23.44, 23.03, 14.45, 14.38, 10.91, 10.83. HR-MS (ESI): Found m/z $[M+H]^+$ 1906.11094; calculated for $C_{114}H_{164}N_6O_6S_6$ 1906.08759.

Data for **3**: ^{1}δH NMR ($CDCl_3$, 300 MHz) 9.05–8.84 (4H, m), 7.65 (2H, d, J = 4.9 Hz), 7.43 (2H, d, J = 4.2 Hz), 7.33–7.28 (1H, m), 7.23–7.18 (1H, m), 4.04 (8H, d, J = 7.1 Hz), 1.92 (4H,s), 1.44–1.07 (8H, m), 1.04–0.67 (26H, m). ^{13}δC NMR ($CDCl_3$, 300 MHz) 161.62, 140.88, 140.55, 139.15, 136.68, 135.58, 130.80, 129.79, 128.50, 125.99, 108.85, 108.14, 46.30, 45.94, 39.31, 39.07, 37.97, 37.75, 31.91, 31.21, 30.05, 29.65, 29.36, 28.50, 28.34, 26.26, 23.63, 23.08, 22.68, 14.12, 10.56. HR-MS (ESI): Found m/z $[M+H]^+$ 1383.87347; calculated for $C_{84}H_{127}N_4O_4S_4$ 1383.87110.

Data for **4**: MALDI-TOF: Found m/z $[M+H]^+$ 1046.4; calculated for $C_{60}H_{79}N_4O_4S_4$ 1046.7.

3. Results and discussion

3.1. Synthesis and characterization

The synthetic route to 6,6′-((2,5-octyldodecyl)-3,6-dioxo-2,3,5,6-tetrahedropyrrolo[3,4-*c*]pyrrole-1,4-diyl)bis([2,2′-bisthiophene]-5′,5-diyl))bis(2,5-bis(2-ethylhexyl)-3-(thiophen-2-yl)-2,5-dihydropyrrolo[3,4-*c*]pyrrole-1,4-dione) (Tri-BTDPP) is shown in Scheme 1. The mono-brominated DPP compound **1** and the bis(-trimethylstannyl) DPP compound **2** were synthesized according to the methods reported in the literature [32,33]. The introduction of the long 2-octyldodecyl side chain on **2** was intended to render the final compound Tri-BTDPP solution-processable. The synthesis of Tri-BTDPP was conducted via Stille cross coupling reaction between **1** and **2** in a 2.1:1 M ratio in toluene under reflux for 60 h in the presence of $Pd_2(dba)_3$/P(*o*-tolyl)$_3$ as a catalyst. Separation of the target product Tri-BTDPP was accomplished by column chromatography, which was not straightforward due to the close polarity of the Tri-BTDPP and a by-product **4**, which was formed by the homo-coupling of compound **1**. First, column chromatography on silica gel using DCM:hexane and then chloroform was conducted to remove compound **3** (26%) and other impurities to yield a crude product (72%), which still contained compound **4**. Further purification was conducted by using a heated (50 °C) silica gel column using a mixture of chloroform and toluene (with a volume ratio of 1:1) as eluent, which enabled separation of Tri-BTDPP and **4**. Pure Tri-BTDPP was obtained in 56% yield, with the molecular structure confirmed by NMR spectroscopy and mass spectrometry. The yield of the homo-coupling dimer by-product **4** was 16%. Compound **4** was characterized by MALDI-TOF mass spectrometry. NMR spectra could not be obtained for **4** due to the strong aggregation tendency of this compound. The $Pd_2(dba)_3$/P(*o*-tolyl)$_3$ catalyst system is commonly used for Stille reactions [34] and particularly for the synthesis of high performance DPP-based polymers [35–38] because of its good air stability and effectiveness [34,36]. Recently, it was found that a notable quantity of a homo-coupling by-product in a Stille coupling reaction of a similar brominated DPP compound formed [39]. The yield of the homo-coupling by-product is strongly dependent on the Pd catalyst used: $Pd(PPh_3)_2Cl_2$ (~33%) > $Pd_2(dba)_3$/P(*o*-tolyl)$_3$ (~11%) > $Pd(PPh_3)_4$ (~6%). However, for the Stille coupling reaction in the presence of $Pd_2(dba)_3$/P(*o*-tolyl)$_3$ in this study, a higher yield of the homo-coupling by-product was formed, thus highlighting that optimization of the synthetic conditions is very important. Therefore, other types of catalysts such as $Pd(PPh_3)_4$ may be used to improve the yields of the target Tri-BTDPP.

Among the solvents tested (hexane, chloroform, toluene, chlorobenzene and *o*-dichlorobenzene), only chloroform provides a solubility above 10 mg mL^{-1} for Tri-BTDPP, which confirms the need of long alkyl chains on the DPP units. This solubility is comparable to that of the Tri-DPP compounds (10–25 mg mL^{-1}) reported by Nguyen et al. [40]. The thermal properties of Tri-BTDPP were studied by differential scanning calorimetry (DSC) (Fig. S8). Tri-BTDPP presents an endothermic peak corresponding to its melting point at 253 °C in the heating scan and an exothermic peak at 232 °C corresponding to its crystallization temperature in the cooling scan.

3.2. Optical properties

The UV–Vis absorption spectra of Tri-BTDPP in chloroform solution and neat film are shown in Fig. 1 Tri-BTDPP absorbs in the range of 600–850 nm in solution with the wavelength of maximum absorption (λ_{max}) at 707 nm. Compared with Tri-DPP compounds containing a central bisphenyl DPP unit, which shows an absorption onset at ~625–670 nm [27,40], Tri-BTDPP presents a much longer absorption onset at ~810 nm. This is due to the increased conjugation length as a result of higher coplanarity and a more efficient intramolecular charge transfer from the electron-donating thiophene units to the central electron-accepting DPP unit. In films, the λ_{max} red-shifts to 725 nm and an additional shoulder at ~830 nm appears. The spectrum extends up to 1000 nm. The red-shift of the absorption spectrum from solution to film originates from the planarization of the molecule and the strong intermolecular interactions in the solid state. The optical band gap (E_g) was calculated from the onset absorption wavelength to be 1.33 eV, which is much lower than its Tri-DPP analogues (E_g = 1.65–1.71 eV) [27,40]. The band gap of Tri-BTDPP is within the range of 1.2 eV–1.7 eV that is needed for optimal harvesting of sunlight to achieve a high PCE [41].

3.3. Electrochemical properties and theoretical calculations

Density functional theory (DFT) calculations were carried out on Tri-BTDPP to study its optimized molecular geometry and energy levels. The B3LYP (Beckes, three-parameter, Lee-Yang-Parr) exchange-correlation functional was employed on the standard 6-31G basis set to define the lowest energy conformation. In addition, methyl side chains were chosen to facilitate the calculation. As shown in Fig. 2, Tri-BTDPP adopts a coplanar structure as the lowest energy conformation, which would be beneficial for intermolecular interactions and potentially close π–π stacking. It can also be seen that the highest occupied molecular orbital (HOMO) and the lowest unoccupied molecular orbital (LUMO) extend over the entire molecule, revealing an efficient conjugation and intramolecular charge transfer (ICT) between thiophene and DPP moieties. The theoretical values of the HOMO and LUMO levels were evaluated to be −4.76 eV and −3.15 eV, respectively, which leads to a band gap of 1.61 eV.

The electrochemical properties of Tri-BTDPP were investigated by cyclic voltammetry (CV) (Fig. S9). The HOMO level was calculated from the onset of the first oxidation peak using the equation: $E_{HOMO} = -(E_{ox}^{onset} - (E_{Fc} - 4.8))$ eV, where −4.8 eV is the HOMO energy level of ferrocene (Fc) [42]. Since no reduction peak was observed, the LUMO was estimated by adding the optical band gap (1.33 eV) to the HOMO. The HOMO and LUMO of Tri-BTDPP were evaluated to be −5.34 eV and −3.99 eV, respectively. In comparison with the energy levels of its Tri-DPP analogues [27,40], Tri-BTDPP

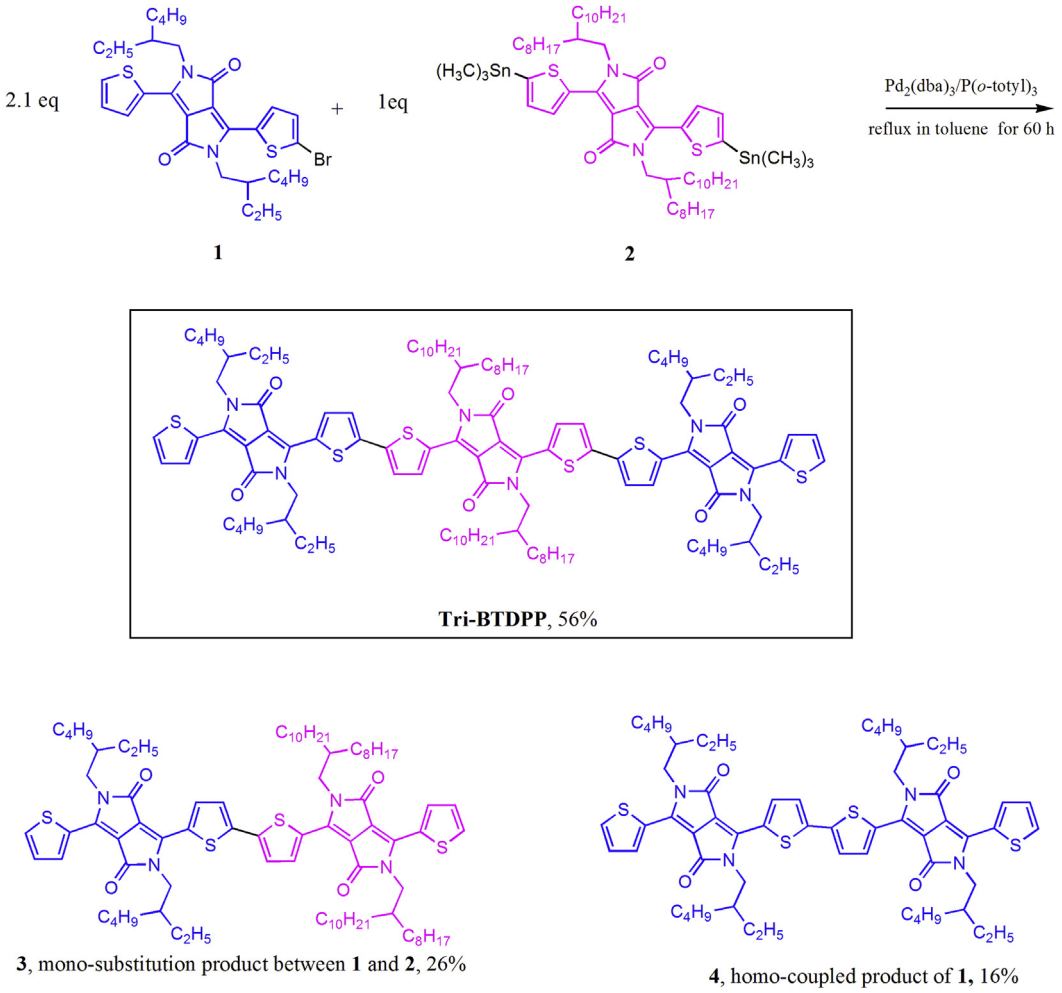

Scheme 1. Synthetic route to Tri-BTDPP via Stille coupling reaction of **1** and **2**.

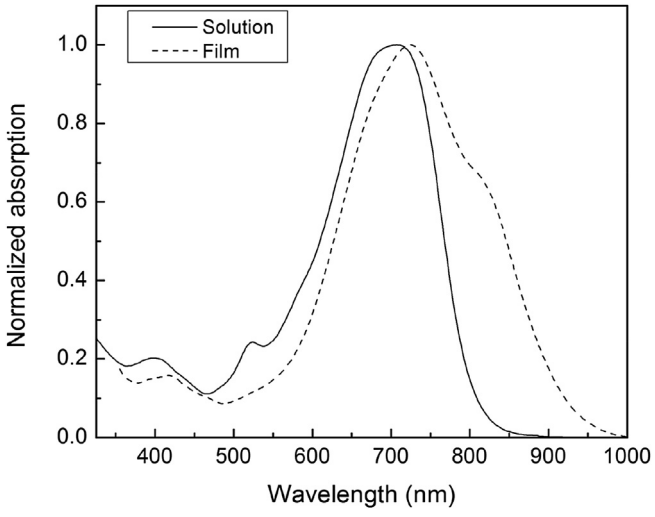

Fig. 1. UV–Vis spectra of Tri-BTDPP in solution and in film.

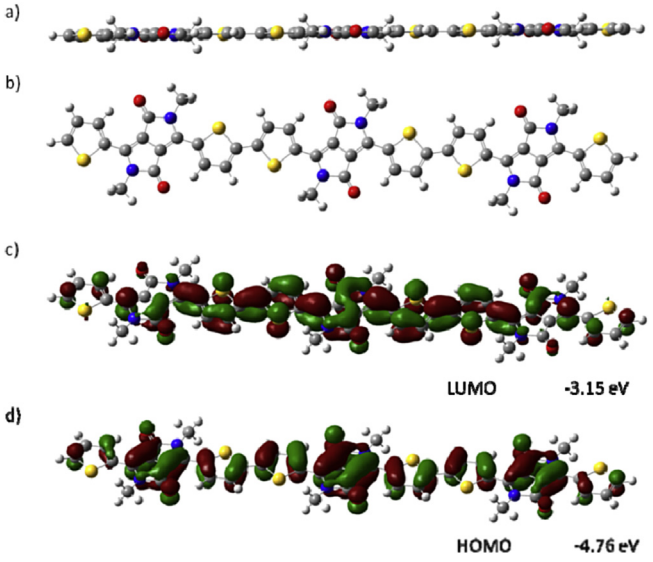

Fig. 2. DFT calculations of Tri-BTDPP: a) and b) conformations at the lowest energy; c) and d) Frontier orbitals.

displays a similar HOMO energy level but a deeper energy LUMO level. The offset between the LUMO of Tri-BTDPP (−3.99 eV) and PCBM (−4.3 eV) [43] was estimated to be 0.3 eV, which is equivalent to the value needed for electron transfer from donor to acceptor with minimal energy loss [41]. Based on Scharber's methods [41], a theoretical V_{oc} value of 0.74 V and a PCE of 10% can

be obtained for a blend of Tri-BTDPP and PCBM confirming that Tri-BTDPP is a promising donor for organic solar cells. However, achieving such a PCE requires the blend layer morphology, charge transport, and several other parameters to be optimal.

3.4. Charge transport and photovoltaic properties

The charge transport property of Tri-BTDPP was studied in bottom-gate bottom-contact field effect transistors (OFETs) using heavily n-doped Si/SiO_2 wafer substrates. The devices showed p-type hole transport performance. The average saturation hole mobility of the as-cast thin films was evaluated to be 1.21×10^{-4} cm^2 V^{-1} s^{-1}. The devices with Tri-BTDPP films annealed at 100 °C and 150 °C for 10 min exhibited higher hole mobilities with an average values of 7.44×10^{-4} cm^2 V^{-1} s^{-1} and 9.41×10^{-4} cm^2 V^{-1} s^{-1}, respectively, indicating improved molecular ordering in the annealed films. Fig. 3 shows the transfer and output curves of the best device, annealed at 150 °C, which shows the highest mobility of 1.22×10^{-3} cm^2 V^{-1} s^{-1}. This value is likely underestimated as the output curves close to the origin ($V_{DS} = 0$ V) are s-shaped due to contact resistance effects. In comparison with Nguyen's Tri-DPP with branched side chains [40], Tri-BTDPP presents a higher hole mobility even with much larger branched alkyl chains on the central DPP core, indicating that the improved backbone coplanairy helped the charge transport. However, Tri-BTDPP's hole mobility remains lower than Tri-DPP with phenyl end-capping units or linear alkyl chains [27,44]. However, linear alkyl chains would not furnish enough solubility to Tri-BTDPP.

The photovoltaic properties of a blend of Tri-BTDPP as a donor and [6,6]-phenyl-C_{61}-butyric acid methyl ester ($PC_{61}BM$) as an acceptor were investigated in bulk heterojunction (BHJ) solar cells. Here, we detail several optimizations made on the device architecture and the blend formulation. First, a conventional architecture, ITO/PEDOT:PSS/Tri-BTDPP:$PC_{61}BM$/Al, was used. The active layer was deposited by spin-coating a solution of Tri-BTDPP:$PC_{61}BM$ in chloroform. Very low PCE values of <0.1% (V_{oc} = 0.36 V; *FF* = 0.28; short circuit current density (J_{sc}) = 0.56 mA cm^{-2}) were obtained. The poor performance was most likely due to a poor morphology, or more specifically, a poor nanophase separation of the donor and acceptor in the films (to be discussed below). Solvent additives are often used to tailor the morphology to improve the solar cell performance [45,46]. We used 1,8-diiodooctane (DIO), which is one of the most commonly used additives, to improve the film morphology of the Tri-BTDPP:$PC_{61}BM$ blend. Different amounts (vol.% relative to the solvent) of DIO (0.25%, 0.5%, 1%, 2%, 3%, 4% and 5%) were added in the blend solution (Fig. S10). With 1% DIO and at optimized active layer thickness (Fig. S11) and Tri-BTDPP/$PC_{61}BM$ ratio (Fig. S12), an improved PCE of 0.27% was obtained, which is, however, still very low. The low PCE was largely due to the low J_{sc} and *FF*, which might originate from the inefficiency of the exciton diffusion, exciton dissociation, charge transport, and/or collection step. In order to improve the electron collection, a thin layer (~10 nm) of calcium (Ca) was introduced between the active layer and the aluminum electrode. Additionally, instead of $PC_{61}BM$, [6,6]-phenyl-C_{71}-butyric acid methyl ester ($PC_{71}BM$) was used because $PC_{71}BM$ often shows better cell performance. The PCE increased to 0.43% due to the improved *FF* (Table 1). Next, an inverted solar cell structure, ITO/ZnO_x/Tri-BTDPP:$PC_{71}BM$/MoO_3/Ag, was adopted to improve the hole collection. Higher J_{sc} of 2.15 mA cm^{-2}, V_{oc} of 0.67 V, and *FF* of 0.50 were achieved, which led to an increased PCE up to 0.72%. However, the cell performance is still relatively low compared to other small molecules reported in the literature, mainly due to the low J_{sc} [47]. In the following section, we investigate the root causes for such low efficiencies.

3.5. Morphology

Organic semiconductors have intrinsically very short exciton diffusion lengths in the range of ~1–10 nm [48,49] due to their large exciton binding energy compared to inorganic semiconductors. Therefore, realizing donor-acceptor phase separation with domain sizes in the range of their diffusion lengths is crucial to achieve high solar cell performance. Atomic force microscopy (AFM) was used on a Tri-BTDPP:$PC_{71}BM$ (1:1) blend film prepared using the same conditions as for the one that achieved the best solar cell performance to elucidate the film morphology and phase separation. As shown in Fig. 4 large grains of ~100–200 nm were observed in both height and phase images. Since the phase image is very similar to the height image, each grain seems uniform in composition. Because the Tri-BTDPP phase is highly crystalline as revealed by the X-ray diffraction (XRD) measurements (to be discussed below), the grains appearing in the AFM images are likely the Tri-BTDPP phase. The $PC_{71}BM$ phase might be present at the boundaries of the Tri-BTDPP (the grain boundaries in the phase image are larger than in the height image). It is also possible that a vertical phase separation occurred with $PC_{71}BM$ enriched at the bottom of the film [50–52]. The increase in J_{sc} observed in the inverted devices compared with the standard devices supports this hypothesis because the charge collection would be more favored for the

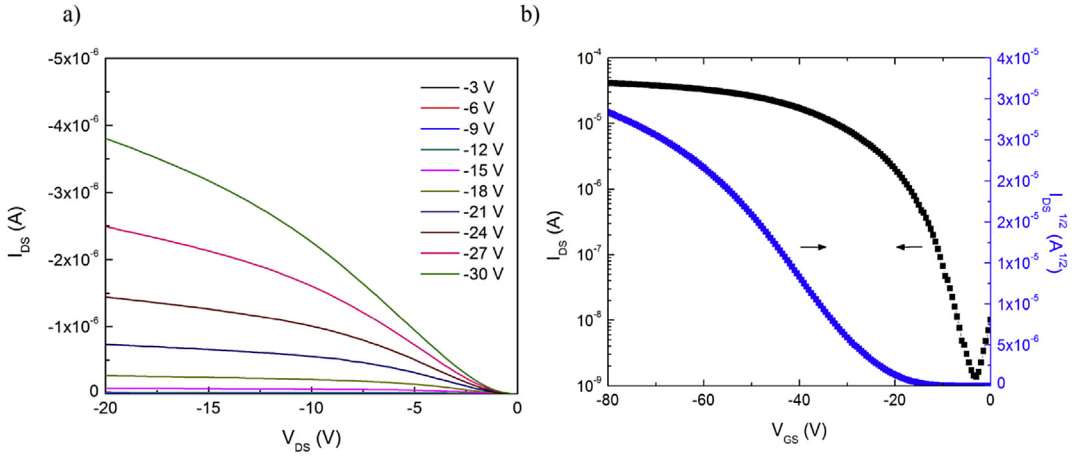

Fig. 3. Field effect transistor characteristics of Tri-BTDPP after annealing at 150 °C: a) output curves and b) transfer curve at $V_{DS} = -30$ V.

Table 1
Photovoltaic performances of Tri-BTDPP:$PC_{61}BM$ or $PC_{71}BM$ blends with different device architectures.

	Architecture	J_{sc} (mA cm^{-2})	V_{oc} (V)	FF	PCE (%)
1	Conventional: ITO/PEDOT:PSS/Tri-BTDPP:$PC_{61}BM$ (1:1)/Al	1.30	0.56	0.38	0.27
2	Conventional: ITO/PEDOT:PSS/Tri-BTDPP:$PC_{71}BM$ (1:1)/Ca/Al	1.61	0.57	0.47	0.43
3	Inverted: ITO/ZnO_x/Tri-BTDPP:$PC_{71}BM$ (1:1)/MoO_3/Ag	2.15	0.67	0.50	0.72

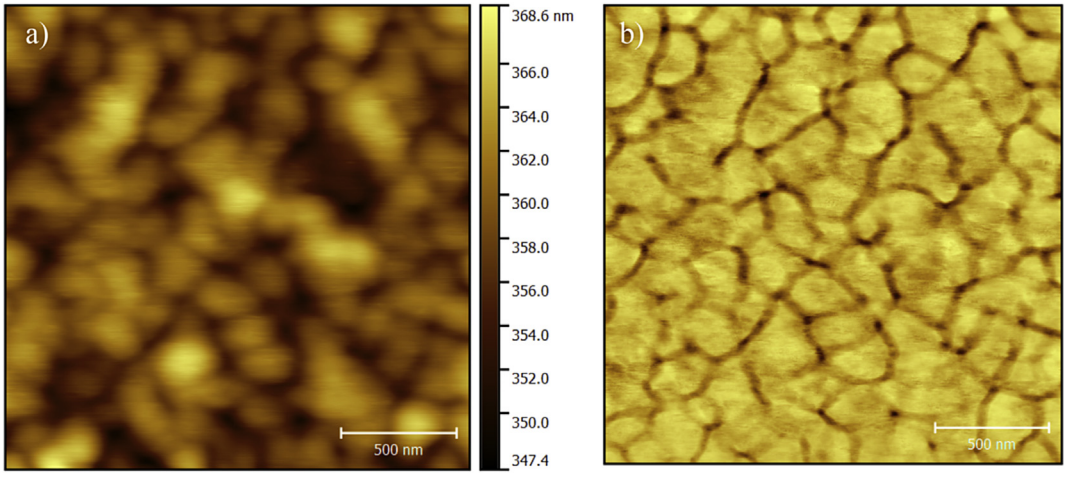

Fig. 4. AFM height (a) and phase (b) images 0.5 μm × 0.5 μm of Tri-BTDPP: $PC_{71}BM$ (1:1) film from chloroform and 1 vol. % DIO solution.

inverted structure if $PC_{71}BM$ is enriched at the bottom and Tri-BTDPP is enriched on the top. The large domain size of the Tri-BTDPP phase (~100–200 nm) greatly exceeded its diffusion length, which is possibly in the range of ~1–10 nm [48,49], making the diffusion of the majority of excitons to the donor/acceptor interface very difficult. This, in turn, would cause poor charge carrier generation due to geminate recombination of excitons and thus a low J_{sc}. A further reduction in the domain size down to the exciton diffusion length is needed to improve the charge generation.

To further understand the formation and composition of the phases of the blend film morphology, the interaction of Tri-BTDPP and $PC_{71}BM$ was investigated using differential scanning calorimetry (DSC). The measurements were completed on films prepared by drop-casting solutions of Tri-BTDPP and $PC_{71}BM$ with different ratios in chloroform. The DSC trace of the first heating scan of each sample is shown in Fig. 5. The melting points of both Tri-BTDPP and $PC_{71}BM$ in their blends do not exhibit a notable melting point depression at all blend ratios, indicating their very low miscibility. This suggests that Tri-BTDPP and $PC_{71}BM$ do not intermix and rather form respective pure domains, which explains the resembling height and phase AFM images. According to previous studies, an ideal donor/acceptor blend layer morphology for OPVs should provide not only pure domains of donor and acceptor to extract the charges but also donor-acceptor intermixed domains for ultrafast charge separation [53–55]. The immiscibility of Tri-BTDPP and $PC_{71}BM$ induces the formation of over-sized pure domains and inhibits the formation of intermixed domains, leading to hampered exciton dissociation and charge separation.

XRD measurements were carried out to study the nature of the molecular packing of the neat Tri-BTDPP and Tri-BTDPP:$PC_{71}BM$ blend films. As shown in Fig. 6, for the Tri-BTDPP neat film, sharp and intense diffraction peaks at $2\theta = 4.50°$, 8.96°, 13.28°, 17.72° and 22.64° are clearly seen. The crystallinity of Tri-BTDPP is much higher than Tri-DPP where the diffraction peaks were barely or not visible [40]. According to the Bragg's law, the first four peaks represent the 1st to 4th order peaks of planes with a *d*-spacing

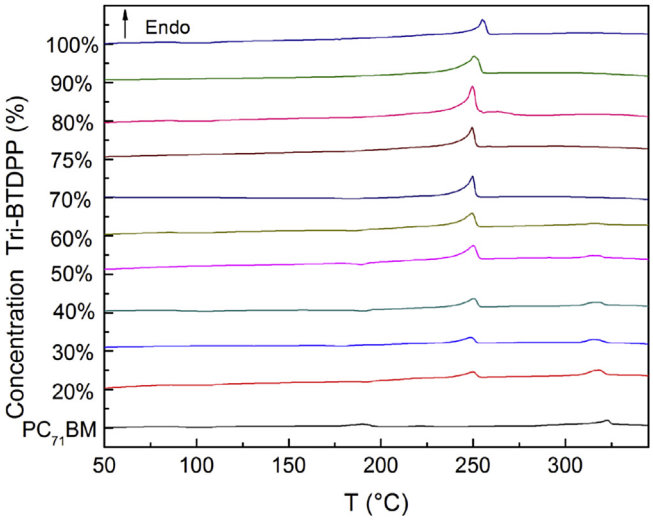

Fig. 5. DSC first heating scans of Tri-BTDPP:$PC_{71}BM$ blend films with different Tri-BTDPP concentrations.

distance of 1.96 nm, while the last peak represents another set of planes with a *d*-spacing distance of 0.39 nm. This XRD pattern is reminiscent of a lamellar packing motif, which has been frequently observed for many crystalline polymers such as regioregular head-to-tail poly(3-hexylthiophene) (P3HT) [56] and a number of DPP polymers [29]. Therefore, it is reasonable to consider that the Tri-BTDPP molecules adopted a lamellar packing motif, with an interlayer distance of 1.96 nm, separated by the alkyl chains, and a π–π stacking distance of 0.39 nm between the conjugated backbones. The size of the crystallites was determined from the primary diffraction peak by the Scherrer equation to be 27.4 nm. For the 1:1 Tri-BTDPP:$PC_{71}BM$ blend film, the primary and secondary diffraction peaks were still observed at the same positions. The size of Tri-BTDPP crystallites remained at 27.4 nm, which confirmed that

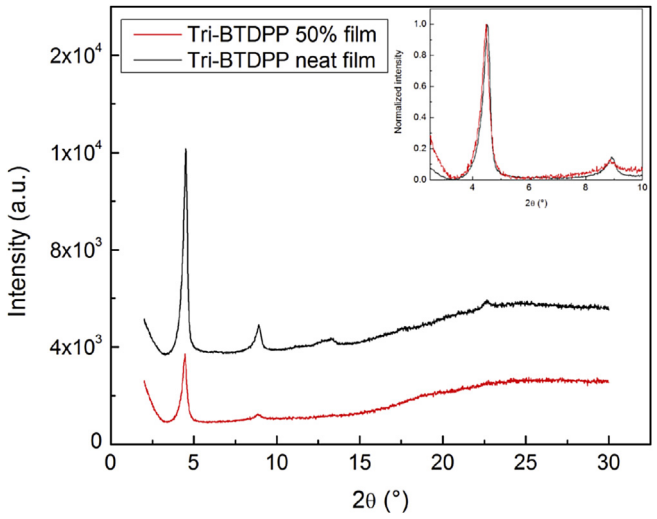

Fig. 6. XRD measurements on Tri-BTDPP neat film and blend with $PC_{71}BM$ (1:1) films.

$PC_{71}BM$ did not intermix with Tri-BTDPP to influence the crystal structure of the Tri-BTDPP phase. The crystallite size of the Tri-BTDPP phase is relatively large compared to the exciton diffusion length and the Tri-BTDPP crystallites may aggregate into even larger domains. To achieve a better morphology for OPVs, the size of Tri-BTDPP's crystallites have to be reduced. In some accounts, nucleating agents were used to increase the number of nuclei and to impede the formation of large crystals [57,58]. Alternatively, side chain engineering, e.g., the use of large side chains on the DPP units, may reduce the crystallite size and improve the morphology of the blend films.

3.6. External quantum efficiency

To further investigate the photovoltaic process within the devices, the external quantum efficiency was measured for the solar cell with an optimal PCE of 0.72%. Fig. 7 shows that the current was mainly generated in the range from 300 nm to 600 nm. This spectrum region corresponds to the $PC_{71}BM$ absorption band, indicating that the current is mainly resulted from the excitons formed within $PC_{71}BM$. The lack of Tri-BTDPP's exciton contribution can be explained by the unfavorable morphology that hinders exciton diffusion and charge separation as discussed above.

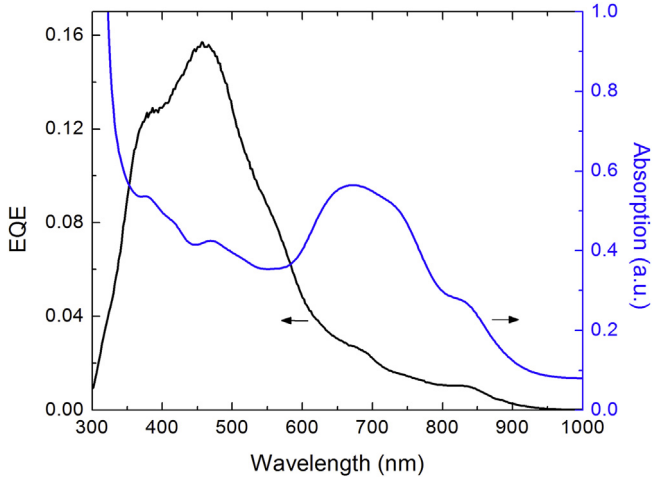

Fig. 7. EQE and absorption spectra of a Tri-BTDPP:$PC_{71}BM$ (1:1) blend.

4. Conclusion

A new oligomeric semiconductor containing three bisthiophene-DPP units (Tri-BTDPP) was designed and synthesized. The extended π-conjugation and strong intramolecular charge transfer of Tri-BTDPP induced a broad absorption up to the near infrared region (~1000 nm). Tri-BTDPP demonstrated a good hole mobility up to 1.22×10^{-3} $cm^2 V^{-1} s^{-1}$ in solution-processed OFETs. As an electron donor semiconductor in organic solar cells, Tri-BTDPP exhibited a PCE of 0.72%. AFM, DSC, and XRD analysis revealed that Tri-BTDPP and $PC_{71}BM$ were unable to intermix effectively, resulting in oversized Tri-BTDPP crystalline phases that are detrimental for exciton diffusion. The unfavored nanophase separation could explain the relatively poor cell performance despite the rather desirable optical and electronic properties of the donor semiconductor. To improve the solar cell performance of Tri-BTDPP, sub-10 nm crystallite sizes and a better mixing with the acceptor need to be achieved by either modification of its chemical structure such as side chains or exploration of other processing conditions.

Acknowledgments

This work was financially supported by the University of Bordeaux and SOLVAY in framework of IDS-FUNMAT network (2012-14-LF). We would like to acknowledge Bertrand Pavageau, Marie-Béatrice Madec and Bin Sun for their contributions to this work. Jaime Martín acknowledges support from the European Union's Horizon 2020 research and innovation programme under the Marie Skłodowska-Curie grant agreement No. 654682.

Appendix A. Supplementary data

Supplementary data related to this article can be found at http://dx.doi.org/10.1016/j.dyepig.2016.04.002.

References

[1] Petritsch K, Dittmer J, Marseglia E, Friend R, Lux A, Rozenberg G, et al. Dye-based donor/acceptor solar cells. Sol Energy Mater Sol Cells 2000;61:63–72. http://dx.doi.org/10.1016/S0927-0248(99)00097-5.
[2] Riede M, Mueller T, Tress W, Schueppel R, Leo K. Small-molecule solar cells-status and perspectives. Nanotechnology 2008;19:424001. http://dx.doi.org/10.1088/0957-4484/19/42/424001.
[3] Mishra A, Bäuerle P. Small molecule organic semiconductors on the move: promises for future solar energy technology. Angew Chem Int Ed Engl 2012;51:2020–67. http://dx.doi.org/10.1002/anie.201102326.
[4] Li Y, Guo Q, Li Z, Pei J, Tian W. Solution processable D–A small molecules for bulk-heterojunction solar cells. Energy Environ Sci 2010;3:1427. http://dx.doi.org/10.1039/c003946b.
[5] Lin Y, Li Y, Zhan X. Small molecule semiconductors for high-efficiency organic photovoltaics. Chem Soc Rev 2012;41:4245–72. http://dx.doi.org/10.1039/c2cs15313k.
[6] Günes S, Neugebauer H, Sariciftci NS. Conjugated polymer-based organic solar cells. Chem Rev 2007;107:1324–38. http://dx.doi.org/10.1021/cr050149z.
[7] Krebs FC. Fabrication and processing of polymer solar cells: a review of printing and coating techniques. Sol Energy Mater Sol Cells 2009;93:394–412. http://dx.doi.org/10.1016/j.solmat.2008.10.004.
[8] Li G, Zhu R, Yang Y. Polymer solar cells. Nat Photonics 2012;6:153–61. http://dx.doi.org/10.1038/nphoton.2012.11.
[9] Mayer AC, Scully SR, Hardin BE, Rowell MW, McGehee MD. Polymer-based solar cells. Mater Today 2007;10:28–33. http://dx.doi.org/10.1016/S1369-7021(07)70276-6.
[10] Chen J-D, Cui C, Li Y-Q, Zhou L, Ou Q-D, Li C, et al. Single-junction polymer solar cells exceeding 10% power conversion efficiency. Adv Mater 2015;27:1035–41. http://dx.doi.org/10.1002/adma.201404535.
[11] Liao S-H, Jhuo H-J, Yeh P-N, Cheng Y-S, Li Y-L, Lee Y-H, et al. Single junction inverted polymer solar cell reaching power conversion efficiency 10.31% by employing dual-doped zinc oxide nano-film as cathode interlayer. Sci Rep 2014;4:6813. http://dx.doi.org/10.1038/srep06813.
[12] Deing KC, Mayerhöffer U, Würthner F, Meerholz K. Aggregation-dependent photovoltaic properties of squaraine/PC61BM bulk heterojunctions. Phys Chem Chem Phys 2012;14:8328–34. http://dx.doi.org/10.1039/c2cp40789b.

[13] Zhang Q, Kan B, Liu F, Long G, Wan X, Chen X, et al. Small-molecule solar cells with efficiency over 9%. Nat Photonics 2014;9:35–41. http://dx.doi.org/10.1038/nphoton.2014.269.
[14] Sun Y, Welch GC, Leong WL, Takacs CJ, Bazan GC, Heeger AJ. Solution-processed small-molecule solar cells with 6.7% efficiency. Nat Mater 2012;11:44–8. http://dx.doi.org/10.1038/nmat3160.
[15] Wang J-L, Yin Q-R, Miao J-S, Wu Z, Chang Z-F, Cao Y, et al. Rational design of small molecular donor for solution-processed organic photovoltaics with 8.1% efficiency and high fill factor via multiple fluorine substituents and thiophene bridge. Adv Funct Mater 2015;25:3514–23. http://dx.doi.org/10.1002/adfm.201500190.
[16] Liu Y, Chen C-C, Hong Z, Gao J, Yang YM, Zhou H, et al. Solution-processed small-molecule solar cells: breaking the 10% power conversion efficiency. Sci Rep 2013;3:3356. http://dx.doi.org/10.1038/srep03356.
[17] He Z, Zhong C, Su S, Xu M, Wu H, Cao Y. Enhanced power-conversion efficiency in polymer solar cells using an inverted device structure. Nat Photonics 2012;6:593–7. http://dx.doi.org/10.1038/nphoton.2012.190.
[18] Huang Y, Guo X, Liu F, Huo L, Chen Y, Russell TP, et al. Improving the ordering and photovoltaic properties by extending π-conjugated area of electron-donating units in polymers with D-A structure. Adv Mater 2012;24:3383–9. http://dx.doi.org/10.1002/adma.201200995.
[19] Chen HC, Chen YH, Liu CC, Chien YC, Chou SW, Chou PT. Prominent short-circuit currents of fluorinated quinoxaline-based copolymer solar cells with a power conversion efficiency of 8.0%. Chem Mater 2012;24:4766–72. http://dx.doi.org/10.1021/cm302861s.
[20] Wallquist O. Diketopyrrolopyrrole (DPP) pigments, in high performance pigments. Weinheim, FRG: Wiley-VCH Verlag GmbH & Co. KGaA; 2001. http://dx.doi.org/10.1002/3527600493.ch11.
[21] Tamayo AB, Walker B, Nguyen T-Q. A low band gap, solution processable oligothiophene with a diketopyrrolopyrrole core for use in organic solar cells. J Phys Chem C 2008;112:11545–51. http://dx.doi.org/10.1021/jp8031572.
[22] Liu J, Sun Y, Moonsin P, Kuik M, Proctor CM, Lin J, et al. Tri-diketopyrrolopyrrole molecular donor materials for high-performance solution-processed bulk heterojunction solar cells. Adv Mater 2013;25:5898–903. http://dx.doi.org/10.1002/adma.201302007.
[23] Zhang Y, Xiao M, Su N, Zhong J, Tan H, Wang Y, et al. Efficient strategies to improve photovoltaic performance of linear-shape molecules by introducing large planar aryls in molecular center and terminals. Org Electron 2015;17:198–207. http://dx.doi.org/10.1016/j.orgel.2014.12.004.
[24] Chen M, Fu W, Shi M, Hu X, Pan J, Ling J, et al. An ester-functionalized diketopyrrolopyrrole molecule with appropriate energy levels for application in solution-processed organic solar cells. J Mater Chem A 2013;1:105–11. http://dx.doi.org/10.1039/c2ta00148a.
[25] Huang J, Zhan C, Zhang X, Zhao Y, Lu Z, Jia H, et al. Solution-processed DPP-based small molecule that gives high photovoltaic efficiency with judicious device optimization. Appl Mater Interfaces 2013:2033–9. http://dx.doi.org/10.1021/am302896u.
[26] Loser S, Bruns CJ, Miyauchi H, Ortiz RP, Facchetti A, Stupp SI, et al. A naphthodithiophene-diketopyrrolopyrrole donor molecule for efficient solution-processed solar cells. J Am Chem Soc 2011;133:8142–5. http://dx.doi.org/10.1021/ja202791n.
[27] Liu S-Y, Fu W-F, Xu J-Q, Fan C-C, Jiang H, Shi M, et al. A direct arylation-derived DPP-based small molecule for solution-processed organic solar cells. Nanotechnology 2014;25:014006. http://dx.doi.org/10.1088/0957-4484/25/1/014006.
[28] Tieke B, Rabindranath AR, Zhang K, Zhu Y. Conjugated polymers containing diketopyrrolopyrrole units in the main chain. Beilstein J Org Chem 2010;6:830–45. http://dx.doi.org/10.3762/bjoc.6.92.
[29] Qu S, Tian H. Diketopyrrolopyrrole (DPP)-based materials for organic photovoltaics. Chem Commun 2012;48:3039. http://dx.doi.org/10.1039/c2cc17886a.
[30] Li Y, Sonar P, Murphy L, Hong W. High mobility diketopyrrolopyrrole (DPP)-based organic semiconductor materials for organic thin film transistors and photovoltaics. Energy Environ Sci 2013;6:1684. http://dx.doi.org/10.1039/c3ee00015j.
[31] Liu S-Y, Shi M-M, Huang J-C, Jin Z-N, Hu X-L, Pan J-Y, et al. C–H activation: making diketopyrrolopyrrole derivatives easily accessible. J Mater Chem A 2013;1:2795. http://dx.doi.org/10.1039/c2ta01318e.
[32] Lee J, Jang M, Lee SM, Yoo D, Shin TJ, Oh JH, et al. Fluorinated benzothiadiazole (BT) groups as a powerful unit for high-performance electron-transporting polymers. Appl Mater Interfaces 2014:20390–9. http://dx.doi.org/10.1021/am505925w.
[33] Sahu D, Tsai C-H, Wei H-Y, Ho K-C, Chang F-C, Chu C-W. Synthesis and applications of novel low bandgap star-burst molecules containing a triphenylamine core and dialkylated diketopyrrolopyrrole arms for organic photovoltaics. J Mater Chem 2012;22:7945. http://dx.doi.org/10.1039/c2jm16760c.
[34] Harding BA, Melvin PR, Dougherty W, Kassel S, Goodson FE. Capturing a ghost. Synthesis and structural characterization of Pd(dba)[P(o-Tol)$_3$]$_2$. Organometallics 2013;32:3570–3. http://dx.doi.org/10.1021/om400335a.
[35] Tsai JH, Lee WY, Chen WC, Yu CY, Hwang GW, Ting C. New two-dimensional thiophene-acceptor conjugated copolymers for field effect transistor and photovoltaic cell applications. Chem Mater 2010;22:3290–9. http://dx.doi.org/10.1021/cm100661z.
[36] Li J, Zhao Y, Tan HS, Guo Y, Di C-A, Yu G, et al. A stable solution-processed polymer semiconductor with record high-mobility for printed transistors. Sci Rep 2012;2:754. http://dx.doi.org/10.1038/srep00754.
[37] Sun B, Hong W, Yan Z, Aziz H, Li Y. Record high electron mobility of 6.3 cm^2 V^{-1} s^{-1} achieved for polymer semiconductors using a new building block. Adv Mater 2014;26:2636–42. http://dx.doi.org/10.1002/adma.201305981. 2613.
[38] Chen S, Sun B, Hong W, Aziz H, Meng Y, Li Y. Influence of side chain length and bifurcation point on the crystalline structure and charge transport of diketopyrrolopyrrole-quaterthiophene copolymers (PDQTs). J Mater Chem C 2014;2:2183–90. http://dx.doi.org/10.1039/C3TC32219J.
[39] Hong W, Chen S, Sun B, Arnould M a, Meng Y, Li Y. Is a polymer semiconductor having a "perfect" regular structure desirable for organic thin film transistors? Chem Sci 2015;6:3225–35. http://dx.doi.org/10.1039/C5SC00843C.
[40] Liu J, Sun Y, Moonsin P, Kuik M, Proctor CM, Lin J, et al. Tri-diketopyrrolopyrrole molecular donor materials for high-performance solution-processed bulk heterojunction solar cells. Adv Mater 2013;25:5898–903. http://dx.doi.org/10.1002/adma.201302007.
[41] Scharber MC, Mühlbacher D, Koppe M, Denk P, Waldauf C, Heeger AJ, et al. Design rules for donors in bulk-heterojunction solar cells—towards 10% energy-conversion efficiency. Adv Mater 2006;18:789–94. http://dx.doi.org/10.1002/adma.200501717.
[42] D'Andrade B, Datta S, Forrest S, Djurovich P, Polikarpov E, Thompson ME. Relationship between the ionization and oxidation potentials of molecular organic semiconductors. Org Electron 2005;6:11–20. http://dx.doi.org/10.1016/j.orgel.2005.01.002.
[43] Song S, Jin Y, Park SH, Cho S, Kim I, Lee K, et al. A low-bandgap alternating copolymer containing the dimethylbenzimidazole moiety. J Mater Chem 2010;20:6517–23. http://dx.doi.org/10.1039/c0jm00772b.
[44] Liu J, Sun Y, Moonsin P, Kuik M, Proctor CM, Lin J, et al. Tri-diketopyrrolopyrrole molecular donor materials for high-performance solution-processed bulk heterojunction solar cells. Adv Mater 2013:1–6. http://dx.doi.org/10.1002/adma.201302007.
[45] Perez LA, Chou KW, Love JA, Van Der Poll TS, Smilgies DM, Nguyen TQ, et al. Solvent additive effects on small molecule crystallization in bulk heterojunction solar cells probed during spin casting. Adv Mater 2013;25:6380–4. http://dx.doi.org/10.1002/adma.201302389.
[46] Park JK, Kim C, Walker B, Nguyen T-Q, Seo JH. Morphology control of solution processable small molecule bulk heterojunction solar cells via solvent additives. RSC Adv 2012;2:2232. http://dx.doi.org/10.1039/c2ra01182d.
[47] Huang Q, Li H. Recent progress of bulk heterojunction solar cells based on small-molecular donors. Chin Sci Bull 2013;58:2677–85. http://dx.doi.org/10.1007/s11434-013-5930-z.
[48] Peumans P, Yakimov A, Forrest SR. Small molecular weight organic thin-film photodetectors and solar cells. J Appl Phys 2003;93:3693. http://dx.doi.org/10.1063/1.1534621.
[49] Luhman WA, Holmes RJ. Enhanced exciton diffusion in an organic photovoltaic cell by energy transfer using a phosphorescent sensitizer. Appl Phys Lett 2009;94:153304. http://dx.doi.org/10.1063/1.3120566.
[50] Ruderer MA, Guo S, Meier R, Chiang HY, Körstgens V, Wiedersich J, et al. Solvent-induced morphology in polymer-based systems for organic photovoltaics. Adv Funct Mater 2011;21:3382–91. http://dx.doi.org/10.1002/adfm.201100945.
[51] Karagiannidis PG, Georgiou D, Pitsalidis C, Laskarakis A, Logothetidis S. Evolution of vertical phase separation in P3HT: PCBM thin films induced by thermal annealing. Mater Chem Phys 2011;129:1207–13. http://dx.doi.org/10.1016/j.matchemphys.2011.06.007.
[52] Jo J, Na S-I, Kim S-S, Lee T-W, Chung Y, Kang S-J, et al. Three-dimensional bulk heterojunction morphology for achieving high internal quantum efficiency in polymer solar cells. Adv Funct Mater 2009;19:2398–406. http://dx.doi.org/10.1002/adfm.200900183.
[53] Westacott P, Tumbleston JR, Shoaee S, Fearn S, Bannock JH, Gilchrist JB, et al. On the role of intermixed phases in organic photovoltaic blends. Energy Environ Sci 2013;6:2756–64. http://dx.doi.org/10.1039/c3ee41821a.
[54] Scarongella M, Paraecattil AA, Buchaca-Domingo E, Douglas JD, Beaupré S, McCarthy-Ward T, et al. The influence of microstructure on charge separation dynamics in organic bulk heterojunction materials for solar cell applications. J Mater Chem A 2014;2:6218–30. http://dx.doi.org/10.1039/c3ta15112c.
[55] Li M, Liu J, Cao X, Zhou K, Zhao Q, Yu X, et al. Achieving balanced intermixed and pure crystalline phases in PDI-based non-fullerene organic solar cells via selective solvent additives. Phys Chem Chem Phys 2014;16:26917–28. http://dx.doi.org/10.1039/C4CP04161E.
[56] Sirringhaus H, Brown PJ, Friend RH, Nielsen MM, Bechgaard K, Langeveld-Voss BMW, et al. Two-dimensional charge transport in self-organized, high-mobility conjugated polymers. Nature 1999;401:685–8. http://dx.doi.org/10.1038/44359.
[57] Lindqvist C, Bergqvist J, Feng C, Gustafsson S, Bäcke O, Treat ND, et al. Fullerene nucleating agents: a route towards thermally stable photovoltaic blends. Adv Energy Mater 2014;4:1301437. http://dx.doi.org/10.1002/aenm.201301437.
[58] Sharenko A, Treat ND, Love JA, Toney MF, Stingelin N, Nguyen T. Use of a commercially available nucleating agent to control the morphological development of solution-processed small molecule bulk heterojunction organic solar cells. J Mater Chem A 2014;2:15717–21. http://dx.doi.org/10.1039/C4TA03469D.